Electronic Supplementary Information

for

Mott-Schottky contact synergistically boosts the electroreduction of nitrate to ammonia under low-nitrate concentration

Xiaojuan Zhu,[a,b,‡] Chaoqun Ma,[c,‡] Yi-Chi Wang,[d] Kaiyu Qu,[a,b] Leyang Song,[a,b] Jing Wang,[a,b] Yushuang Gong,[a,b] Xiang Liu,[a,b] Jintao Zhang,[a,*] Qipeng Lu,[c,*] and An-Liang Wang[a,b,*]

[a]Key Laboratory for Colloid and Interface Chemistry Ministry of Education, State Key Laboratory of Crystal Materials, School of Chemistry and Chemical Engineering, Shandong University. Jinan, 250100, Shandong, China

[b]Suzhou Research Institute, Shandong University, Suzhou, 215123, Jiangsu, China

[c]School of Materials Science and Engineering, University of Science and Technology Beijing, Beijing, 100083, China

[d]Beijing National Center for Electron Microscopy and Laboratory of Advanced Materials, School of Materials Science and Engineering, Tsinghua University, Beijing, 100084, China

[‡]These authors contributed equally to this work.

[*]Corresponding author. Email: jtzhang@sdu.edu.cn; qipeng@ustb.edu.cn; alwang@sdu.edu.cn.

Experimental section

Reagents and chemicals. Sodium sulfate (Na_2SO_4), deuterium oxide (D_2O), cobalt chloride hexahydrate ($CoCl_2·6H_2O$), sodium borohydride ($NaBH_4$), polyvinyl pyrrolidone (PVP, MW = 40000), sodium hypochlorite (NaClO), ammonium-^{15}N chloride ($^{15}NH_4Cl$, 98.5%), sodium nitrate-^{15}N (98.5% $Na^{15}NO_3$), tert-butyl alcohol (TBA), maleic acid ($C_4H_4O_4$), sodium salicylate ($C_7H_6O_3Na$), sodium citrate dehydrate ($C_6H_5Na_3O_7·2H_2O$), gold(III) chloride hydrate ($HAuCl_4·4H_2O$), hydrogen peroxide solution (H_2O_2), sodium thiosulfate ($Na_2S_2O_3$), sodium sulfite anhydrous (Na_2SO_3), hydrofluoric acid (HF), ammonium fluoride (NH_4F), dimethyl-1-pyrroline-N-oxide (DMPO), and nitroferricyanide (III) dihydrate ($Na_2Fe(CN)_5NO·2H_2O$) were obtained from Shanghai Macklin Biochemical Co., Ltd. Sodium hydroxide (NaOH), sulfuric acid (H_2SO_4), hydrochloric acid (HCl), and ammonium chloride (NH_4Cl) were purchased from Sinopharm Chemical Reagent Co., Ltd. Ethanol was purchased from Tianjin Fuyu Fine Chemical Co., Ltd. All the reagents were used as received with no further purification. The deionized water (18.2 MΩ) was used in all experiments.

Material synthesis

Preparation of Co-B@CoO_x, Co-B, and CoO_x. 0.47 g of $CoCl_2·6H_2O$ and 2 g of PVP were dissolved in 500 mL of deionized water. Subsequently, 200 mL of fresh $NaBH_4$ solution (0.25 g) was added to the above solution. After being stirred continuously for 3.5 h in an ice bath, the precipitate was collected by centrifugation and washed three times with deionized water to obtain the Co-B@CoO_x.

Co-B was synthesized using the similar method as Co-B@CoO_x except that there was no stirring and ice bath involved. CoO_x was synthesized with the similar methods as Co-B@CoO_x except that the mixture was stirred for 24 h without the use of ice bath.

Preparation of working electrode. The working electrode was prepared by drop-casting the catalyst ink on the pretreated Ni foam (NF). The NF underwent the following pretreatment procedures: Initially, NF (2 cm^2) was sonicated in 3 M HCl for 15 min. Subsequently, the NF was washed with ethanol and deionized water three times. In a typical preparation of the Co-B@CoO_x/NF electrode, a catalyst ink was formulated by combining 20 mg of as-prepared Co-B@CoO_x, 950 μL of water/ethanol mixture (V_{water} : $V_{ethanol}$ = 1 : 1), and 50 μL of Nafion (5 wt%). The resulting catalyst ink was then sonicated for 1 h. Finally, 300 μL of the catalyst ink was slowly dropcasted onto the pretreated NF (mass loading: 3 mg cm^{-2}).

Physicochemical characterizations. X-ray diffraction (XRD) measurements were performed on Rigaku Smartlab powder diffractometer using a Cu Ka radiation (λ = 1.5418 Å). Transmission electron microscopy (TEM) images were taken with a HITACHI H-8100 electron microscopy (Hitachi, Japan) operated at 200 kV. The specific surface area was estimated by the Brunauer-Emmett-Teller (BET) method on Quantachrome instrument. X-ray photoelectron spectroscopy (XPS) measurements were carried out on an ESCALABMK II X-ray photoelectron spectrometer with exciting source of Mg. The binding energy of C 1s peak at 284.8 eV behaved as a reference to calibrate other binging energy. The ultraviolet-visible (UV-vis) absorbance spectra were collected on SHIMADZU UV-1900 spectrophotometer. UV–vis diffuse reflectance spectroscopy (UV–vis DRS) was performed using a UV–vis spectrophotometer (Lambda 950, PerkinElmer). The Fourier transformed infrared (FT-IR) measurement was performed on Perkin-Elmer spectrometer. ^1H nuclear magnetic resonance (NMR) tests were carried out using a Bruker Avance 500 MHz spectrometer. Zeta potential measurements were conducted using the Malvern Zetasizer Nano ZS90 zeta instrument. Differential electrochemical mass spectrometry (DEMS) was recorded

on a quadrupole mass spectrometer (QAS 100, PrismaPlus). X-ray absorption spectroscopy (XAS) was performed at Shanghai Synchrotron Radiation Facility (SSRF).

Electrochemical measurements and product analysis

NO_3RR measurements. The electrocatalytic performance of NO_3^- reduction reaction (NO_3RR) was assessed using an electrochemical station equipped with a three-electrode setup (working electrode: Co-B@CoO_x/NF, reference electrode: saturated Ag/AgCl, and counter electrode: Pt wire) in 0.5 M Na_2SO_4 (pH = 3) with 100 ppm NO_3^--N solution. All potentials were converted to the reversible hydrogen electrode (RHE) ($E_{RHE} = E_{Ag/AgCl} + 0.197 + 0.059 \times pH$). For the electrochemical NO_3RR test, H-type cell separated by a Nafion 211 membrane was employed. The Nafion 211 membrane underwent a pretreatment process, which involved incubation in 5 wt% H_2O_2 solution at 50 °C for 1 h, followed by treatment with 0.1 M H_2SO_4 at 50 °C for 1 h, and subsequently rinsing with deionized water multiple times. Electrochemical impedance spectroscopy (EIS) measurements were performed with a frequency range of 0.01 Hz to 100 kHz at −0.62 V vs. RHE. The Mott-Schottky (M-S) test was conducted by applying a potential range of 0.2 to 1.0 V with an amplitude of 10 mV at a frequency of 10 kHz. Additionally, the first-order kinetic analysis was carried out in the 0.5 M Na_2SO_4 containing 100 ppm NO_3^--N at −0.90 V.

Determination of NO_3^--N concentration. The concentration of NO_3^--N was determined using a colorimetric method. In detail, 50 μL of electrolyte was extracted from the electrolytic cell and diluted to 5 mL. Subsequently, 100 μL of 1 M HCl was added to the above solution. After aging for 15 min, the UV-vis absorption spectra were recorded. The absorbance value (A) was calculated using the formula: $A = A_{220nm}$ -

$2A_{275nm}$. For calibration, a series of NO_3^--N solutions with known concentrations were utilized for calibration ($y = 0.252x + 0.005$, $R^2 = 0.999$).

Determination of NH_4^+-N concentration. The concentration of NH_4^+-N was determined by indophenol blue method. Firstly, 20 μL of electrolyte was extracted from the electrolytic cell and diluted to 2 mL. Then, 2 mL of chromogenic agent (1.0 M NaOH, $C_7H_6O_3Na$ and 5 wt% $C_6H_5Na_3O_7 \cdot 2H_2O$), 1 mL of oxidizing agent (0.05 M NaClO), and 0.2 mL of 1 wt% $Na_2Fe(NO)(CN)_5 \cdot 2H_2O$, were added to the above solution. After incubation for 1 h, the concentration of NH_4^+-N was calculated based on the absorbance measured at a wavelength of 655 nm, using a standard curve ($y = 0.636x + 0.100$, $R^2 = 0.999$), generated with standard NH_4^+-N solutions with certain concentrations.

Performance evaluation index of electrocatalyst

NO_3^- removal. NO_3^- removal ($R_{NO_3^-}$) is calculated using the following equation:

$$R_{NO_3^-} = \frac{\Delta c_{NO_3^- - N}}{c_0} \times 100\%$$

where c_0 is the initial concentration of NO_3^--N in ppm, $\Delta c_{NO_3^- - N}$ is the concentration change of NO_3^--N before and after electrolysis in ppm.

NH_3 selectivity. NH_3 selectivity (S_{NH_3}) is obtained using the following equation:

$$S_{NH_3} = \frac{c_{NH_3 - N}}{\Delta c_{NO_3^- - N}} \times 100\%$$

where $\Delta c_{NO_3^- - N}$ is the concentration change of NO_3^--N before and after electrolysis in ppm, $c_{NH_3 - N}$ is the measured concentration of $NH_3 - N$ in ppm.

NH_3 yield rate. NH_3 yield rate (Y_{NH_3}, mg h^{-1} cm^{-2}) is calculated using the following equation:

$$Y_{NH_3} = \frac{c_{NH_3} \times V}{t \times S}$$

where c_{NH_3} is the measured NH_3 concentration in ppm, V is the volume of cathode electrolyte in L, t is the reduction time in h, *S* is the geometric area of working electrode in cm^2.

Faradaic efficiency. The NH_3 Faradaic efficiency (FE_{NH_3}) is calculated using the following equation:

$$FE_{NH_3} = \frac{8 \times F \times c_{NH_3} \times V}{17 \times Q} \times 100\%$$

where F is the Faradaic constant (96485 C mol^{-1}), c_{NH_3} is the measured NH_3 concentration in ppm, V is the volume of the cathode electrolyte in L, Q is the total charge passing through the electrode in C.

Energy consumption. The energy consumption (EC) ($kWh\ mol_{NO_3^-}^{-1}$) is calculated using the following equation:

$$EC = \frac{(1.23 - E) \times Q \times 10^{-3}}{V \times \Delta c_{NO_3^- - N}}$$

where E is the applied potential (V), Q is the total charge passing through the electrode, V is the volume of cathode electrolyte (L), $\Delta c_{NO_3^- - N}$ is the concentration change of NO_3^--N before and after electrolysis.

Electric energy per order. The electric energy per order (E_{EO})[1] represents the required energy to reduce the concentration of NO_3^--N by one order of magnitude in a unit volume (kWh m^{-3}), which is calculated according to the following equation:

$$E_{EO} = \frac{(1.23 - E) \times Q \times 10^{-3}}{V \times \log(\Delta c_{NO_3^- - N})}$$

where E is the applied potential (V), Q is the total charge passing through the electrode, V is the volume of cathode electrolyte (m^3), $\Delta c_{NO_3^- - N}$ is the concentration change of NO_3^--N before and after electrolysis.

Half-cell energy efficiency. The half-cell energy efficiency (EE_{NH_3}) is defined as the ratio of fuel energy to applied electrical power, which is calculated using the following equation:

$$EE_{NH_3} = \frac{(1.23 - E^0_{NH_3}) \times FE_{NH_3}}{1.23 - E}$$

where $E^0_{NH_3}$ represents the equilibrium potential of NO_3RR (0.69 V), E is the applied potential.

Apparent rate constant. Apparent rate constant is calculated using the following equation:

$$k_{ap}t = -\ln(\frac{c_t}{c_0})$$

where k_{ap} is the apparent rate constant, t is reaction time, c_0 is the initial concentration of NO_3^--N in ppm), and c_t is the concentration of NO_3^--N after a period of electrolysis time in ppm.

Calculation of ECSA. The ECSA of the working electrode is calculated according to the following equation:

$$ECSA = \frac{C_{dl}}{C_s}$$

where C_s is the specific capacitance for a flat metallic surface (40 μF cm^{-2}), C_{dl} is the double-layer capacitance, which can be calculated by the cyclic voltammetry (CV)

curve in the non-Faradic potential range[2] with scan rates ranging from 20 to 120 mV s^{-1} according to the following formula:

$$I = C_{dl} \times v$$

where I is the half of the difference in the anodic and cathodic current($I = (I_a - I_c)/2$), v is the scan rate, C_{dl} is the double-layer capacitance.

Y_{NH_3} is normalized to ECSA according to the following equation:

$$Y_{NH_3} = \frac{c_{NH_3} \times V}{t \times ECSA}$$

where V is the volume of the cathode electrolyte for NH_3 collection in L, t is the reduction time in h, c_{NH_3} is the measured NH_3 concentration in ppm.

***In-situ* Raman spectroscopy measurements.** *In situ* Raman spectroscopy measurements were carried out by Gamry Refence 3000 + iRaman with a 532 nm laser. A homemade three-electrode cell was used with 0.5 M Na_2SO_4 and 100 ppm NO_3^--N solution as electrolyte. All spectra were collected during chronoamperometric measurements at different potentials.

Electron spin resonance spectroscopy (ESR) experiments. The chronoamperometry test was performed at −0.75 V for 3 min in 0.5 M Na_2SO_4 solution (pH = 3) with and without 100 ppm NO_3^--N. Subsequently, 0.8 mL electrolyte was extracted from the electrolytic cell and 25 mg DMPO was added immediately for ESR measurement.

In-situ attenuated total reflection surface enhanced infrared adsorption spectroscopy (ATR-SEIRAS) experiments. *In-situ* ATR-SEIRAS was performed by an INVENIO S FT-IR spectrometer, equipped with liquid nitrogen cooled MCT detector. Au-coated Si prism (20 mm in diameter) was used as the conductive substrate (working electrode), a Pt foil and an Ag/AgCl electrode were served as counter

electrode and reference electrode, respectively. All spectra were recorded during chronoamperometry tests at different potentials in 0.5 M Na_2SO_4 solution with 100 ppm NO_3^--N.

Online DEMS experiments. The mass spectrometer and an electrochemical workstation were employed for online DEMS measurements. 0.5 M Na_2SO_4 electrolyte with 100 ppm NO_3^--N was kept flowing into a homemade electrochemical cell using a peristaltic pump. Co-B@CoO_x loaded on glassy carbon electrode was used as the working electrode, while Pt wire served as the counter electrode and Ag/AgCl was used as the reference electrode. Chronoamperometry at −0.90 V was performed for 100 s, during which the corresponding mass signals were detected. After completing the chronoamperometry test and ensuring that the mass signals returned to baseline, the next cycle was initiated under the same conditions to minimize errors. After six cycles, the measurement was ended.

Isotope labeling experiments. To investigate the source of NH_3, isotopic labeling experiments were conducted using 98.5% $Na^{15}NO_3$ as the N source. The electrolyte containing $^{15}NH_4^+$ was extracted, and the pH of solution was adjusted to be weakly acid by adding 4 M H_2SO_4. Subsequently, 50 μL of D_2O containing 4.4 mg mL^{-1} $C_4H_4O_4$ was added to the acidified solution (0.5 mL) for NMR test. A calibration curve was generated using a standard $^{15}NH_4^+$ solution, plotting the concentration of $^{15}NH_4^+$-^{15}N against the peak area ratio between $^{15}NH_4^+$-^{15}N and $C_4H_4O_4$.

NO_3^- adsorption experiments. To determine the adsorption capacities of NO_3^- on Co-B, Co-B@CoO_x, and CoO_x, 5 mg of samples were immersed in the electrolyte containing 100 ppm NO_3^--N and stirred for 5 min. The adsorption capacity (q_e) is calculated using the following equation:

$$q_e = \frac{\Delta c_{NO_3^- - N} \times V}{14 \times m}$$ where q_e represents the adsorption capacity ($\mu mol\ mg_{cat.}^{-1}$), $\Delta c_{NO_3^- - N}$ is the concentration change of NO_3^--N before and after electrolysis in ppm, V is the volume of the electrolyte in mL, m is the mass of the catalysts in mg.

H_2O adsorption experiments. For the H_2O adsorption test, the three samples were subjected to moisture exposure for 10 min using a humidifier, Afterward, the samples with absorbed H_2O were analyzed using FT-IR.

TBA quencher experiments. TBA quencher experiments were performed at −0.90 V in 0.5 M Na_2SO_4 containing 100 ppm NO_3^--N. Prior to the experiments, the electrolytes were supplemented with various concentrations of TBA (0.12 M, 0.24 M, 0.36 M).

Rechargeable Zn-NO_3^- battery measurements. The rechargeable Zn-nitrate battery test was conducted in an H-cell divided by a Nafion 211 membrane. The anode compartment contains 1 M KOH as the electrolyte, while the cathode compartment employs 0.5 M Na_2SO_4 with 100 ppm NO_3^--N. The cathode compartment was enclosed in a closed system. A polished zinc plate (2 cm^2) served as the anode, Co-B@CoO_x on carbon paper was used as the cathode.

Computational details. Density functional theory (DFT) calculations were performed by the Vienna *ab-initio* Simulation Package software.[3,4] The pseudo potential, Perdew-Burke-Ernzerhof (PBE), and generalized gradient approximation exchange-correlation function were used.[5,6] The projector augmented wave method was applied to describe the interactions between ions and electrons.[7] The plane-wave cutoff energy basis was set as 450 eV. The DFT-D3 method was employed to describe the van der Waals interactions.[8,9] In the structure optimization process, the 2×2×1 Monkhoest-Pack k-

point mesh was applied to all samples. The energy difference within 10^{-5} eV and force convergence threshold of 0.05 eV $Å^{-1}$ were selected. A vacuum of 15 Å was adopted along the z-axis. To simulate the amorphous structure of Co-B and CoO_x, the supercell models of Co_2B and Co_3O_4 were relaxed by 5 ps (5000 steps for calculations) at 1500 and 1300 K, respectively, using molecular dynamics methods. The simulation time of 5 ps ensures that the system reaches the thermal equilibrium state. The amorphous structure of Co-B@CoO_x was simulated by positioning 4-layered Co-B (3×1) unit cells on 2-layered CoO_x (1×1) unit cells. The electronic occupancies were performed using Gaussian smearing with a width of 0.20 eV. The strong Coulomb coupling of transition metals was taken into account in the description of d-orbitals by using the GGA + U method, in which the U value was 3.5 eV. The free energy change (ΔG) of each elementary reaction can be computed by the following equation:

$$\Delta G = \Delta E + \Delta ZPE - T\Delta S$$

where ΔE, ΔZPE, T, and ΔS are the reaction energy difference, zero-point energy change, temperature, and entropy change, respectively.

Supporting Figures

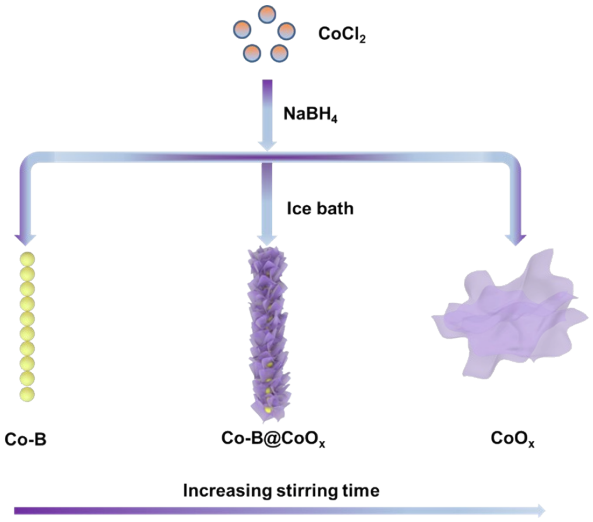

Fig. S1. Illustration of the formation of Co-B, Co-B@CoO_x, and CoO_x.

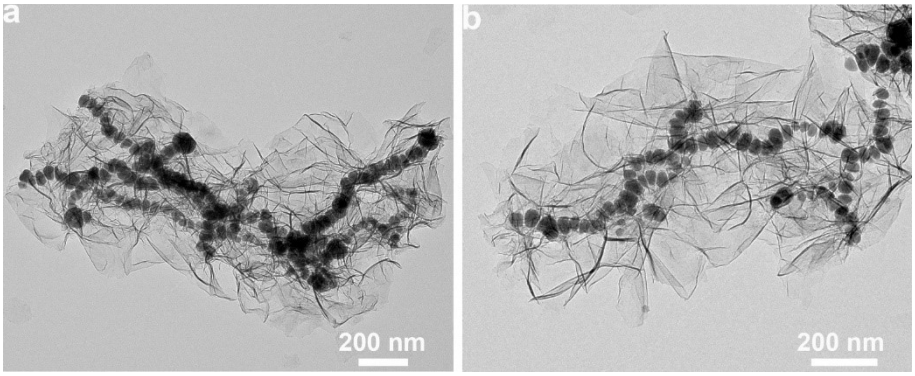

Fig. S2. (a,b) Low-magnification TEM images of Co-B@CoO_x.

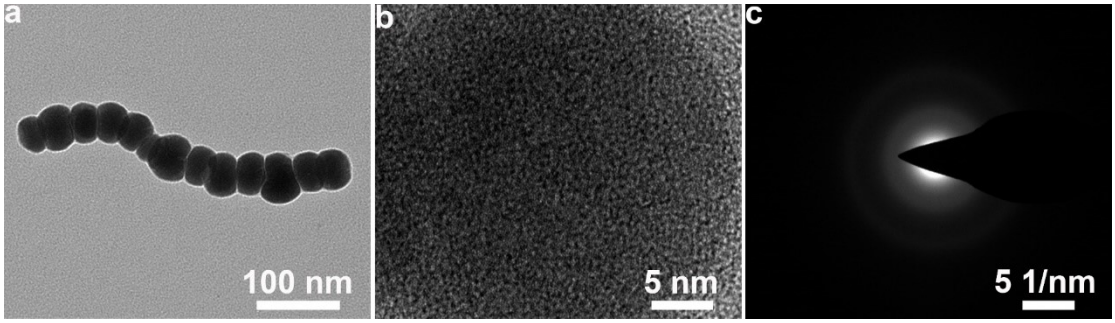

Fig. S3. (a) TEM image, (b) HRTEM image, and (c) SAED pattern of Co-B.

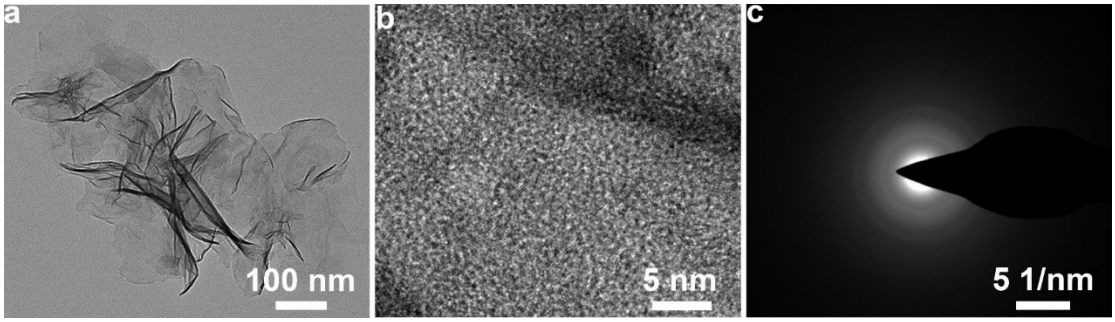

Fig. S4. (a) TEM image, (b) HRTEM image, and (c) SAED pattern of CoO_x.

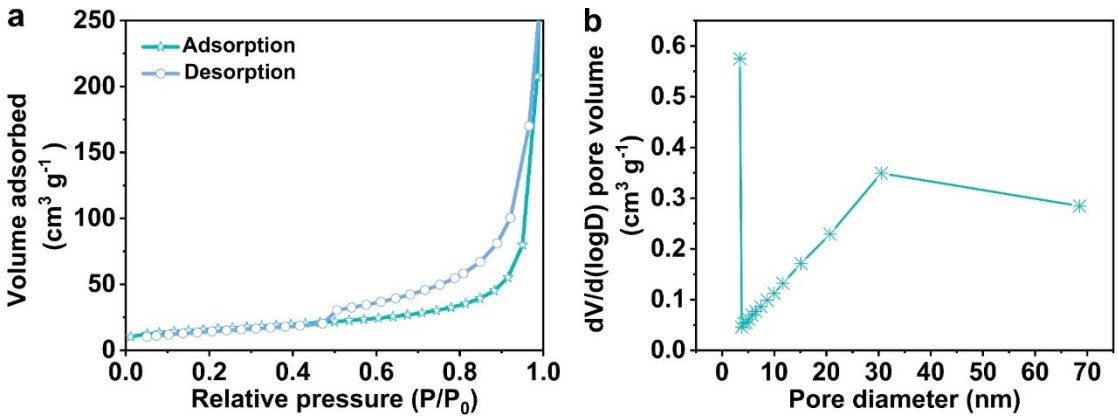

Fig. S5. (a) N_2 adsorption-desorption isotherms and (b) corresponding pore size distribution curve of Co-B@CoO_x.

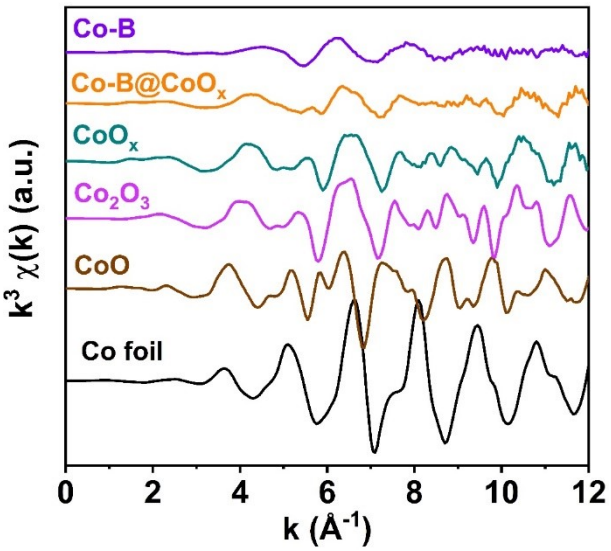

Fig. S6. EXAFS spectra in k space of Co-B, Co-B@CoO_x, CoO_x, Co_2O_3, CoO, and Co foil.

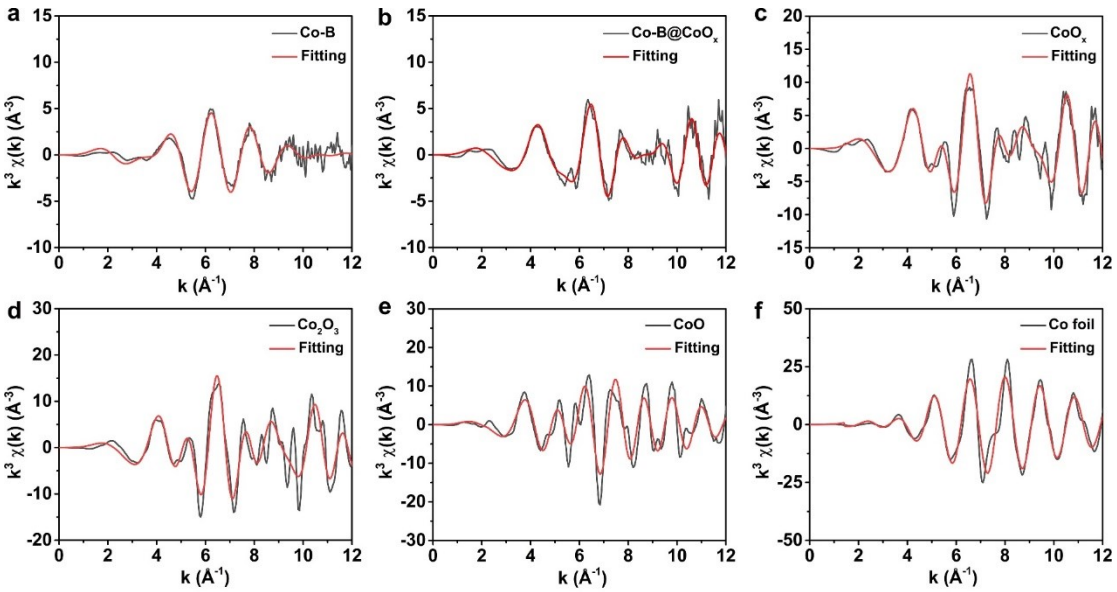

Fig. S7. EXAFS fitting spectra in k-space of (a) Co-B, (b) Co-B@CoO_x, (c) CoO_x, (d) Co_2O_3, (e) CoO, and (f) Co foil.

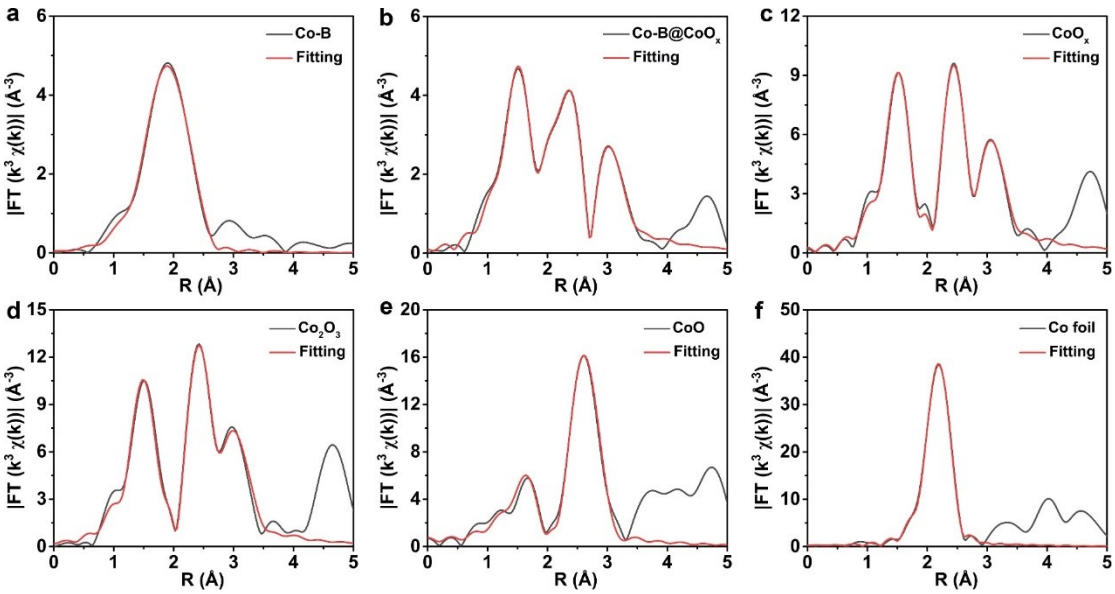

Fig. S8. EXAFS fitting spectra at Co-K edge of (a) Co-B, (b) Co-B@CoO_x, (c) CoO_x, (d) Co_2O_3, (e) CoO, and (f) Co foil.

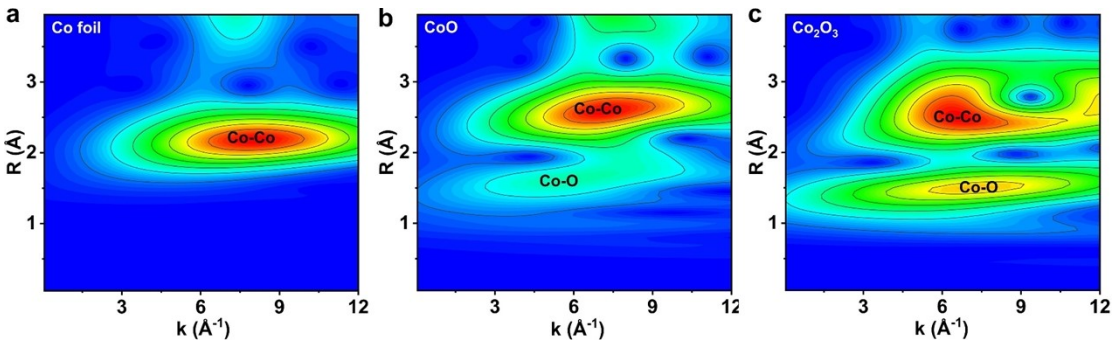

Fig. S9. WT-EXAFS contour plots of (a) Co foil, (b) CoO, and (c) Co_2O_3.

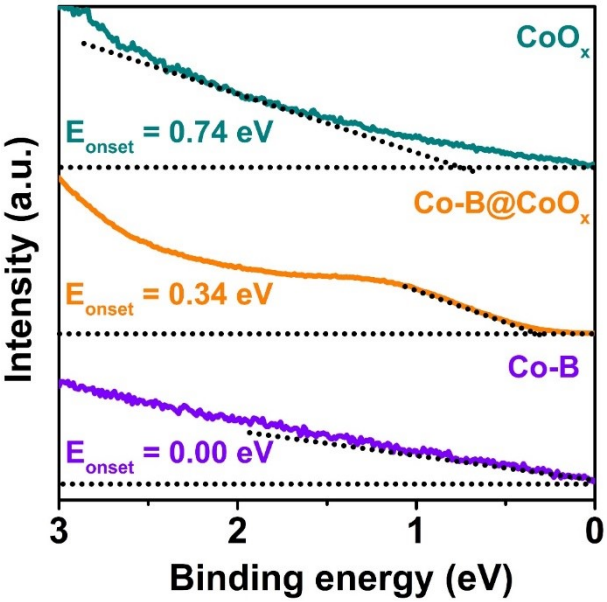

Fig. S10. UPS spectra in the onset energy region of Co-B, Co-B@CoO_x, and CoO_x.

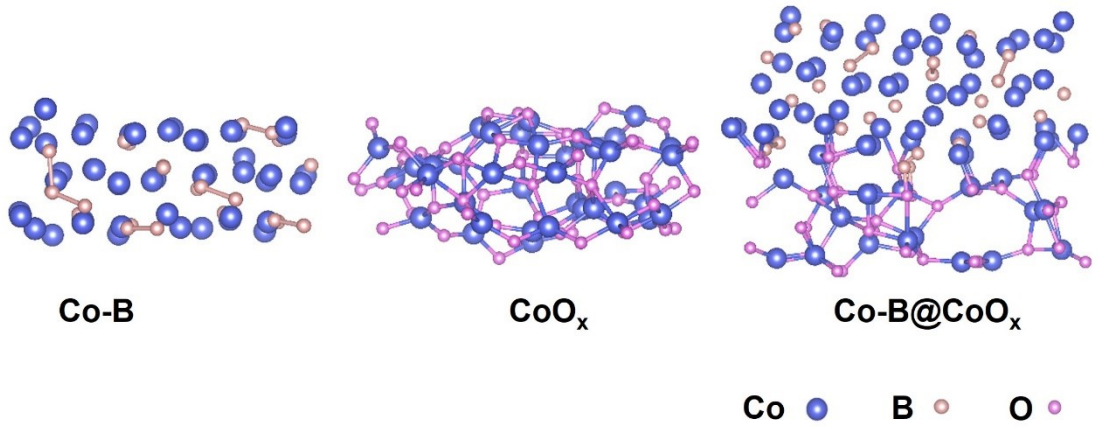

Fig. S11. Optimized structure models of Co-B, CoO_x, and Co-B@CoO_x.

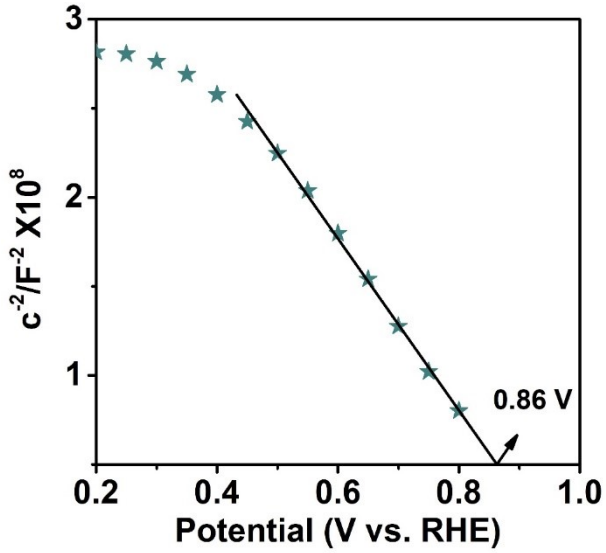

Fig. S12. M-S plot of CoO_x.

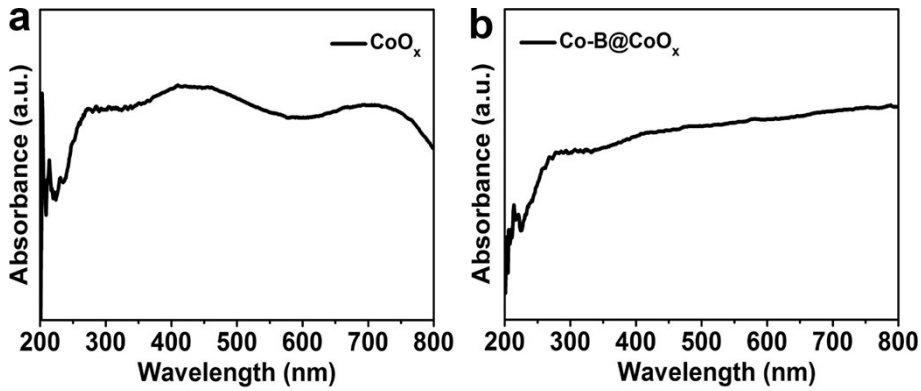

Fig. S13. UV-vis DRS spectra of (a) CoO_x and (b) Co-B@CoO_x.

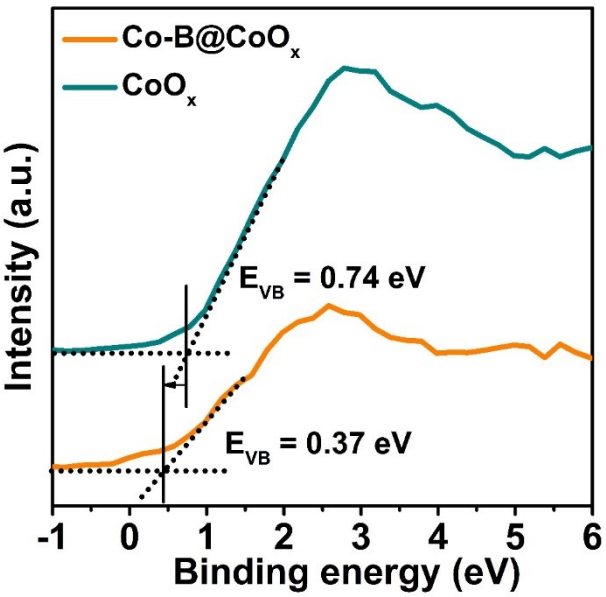

Fig. S14. XPS valence band spectra of Co-B@CoO_x and CoO_x.

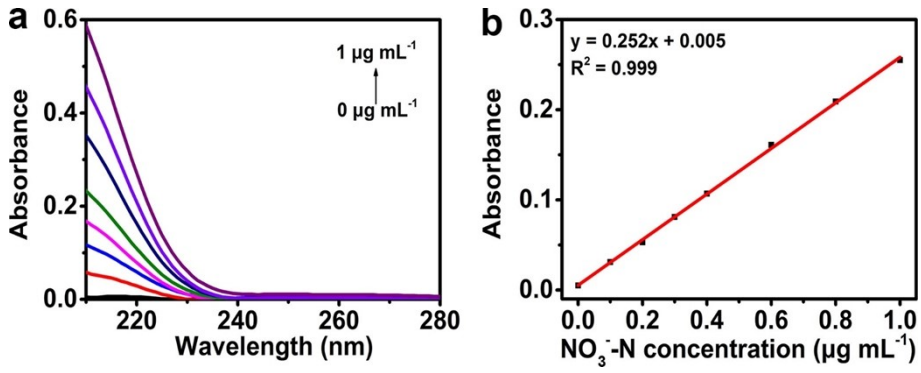

Fig. S15. (a) UV-vis absorption spectra of acidified NO_3^--N solutions with different concentrations. (b) Calibration curve used for the determination of NO_3^--N concentration.

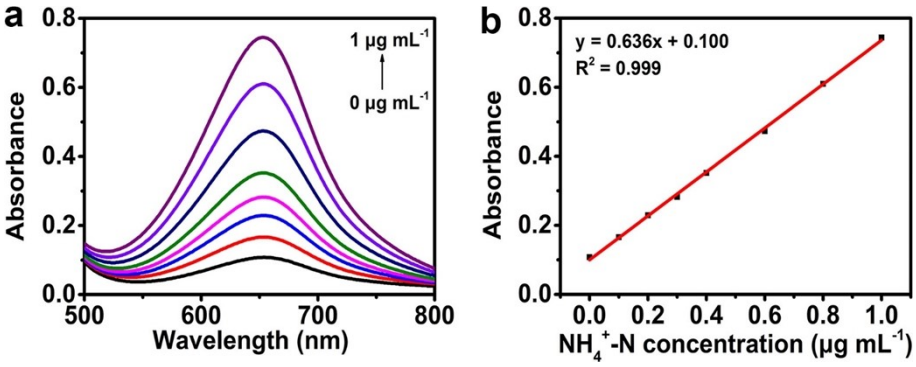

Fig. S16. (a) UV-vis absorption spectra of NH_4^+-N solution with different concentrations. (b) Calibration curve used for the determination of NH_4^+-N concentration.

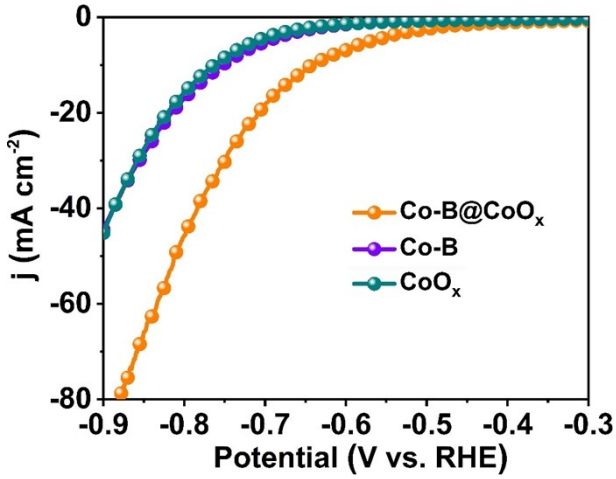

Fig. S17. LSV curves of Co-B@CoO_x, Co-B, and CoO_x in 0.5 M Na_2SO_4 with 100 ppm NO_3^--N.

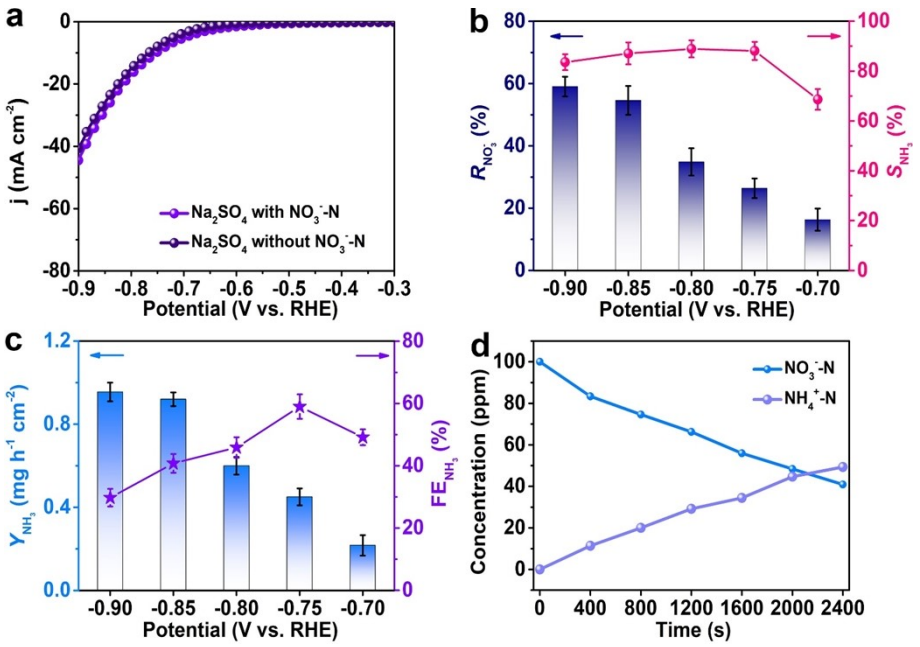

Fig. S18. (a) LSV curves of Co-B in 0.5 M Na_2SO_4 with and without 100 ppm NO_3^--N. (b) $R_{NO_3^-}$ and S_{NH_3} of Co-B at different potentials. (c) Y_{NH_3} and FE_{NH_3} of Co-B at different potentials. (d) Time-dependent concentration change of NO_3^--N and NH_4^+-N over Co-B at −0.90 V.

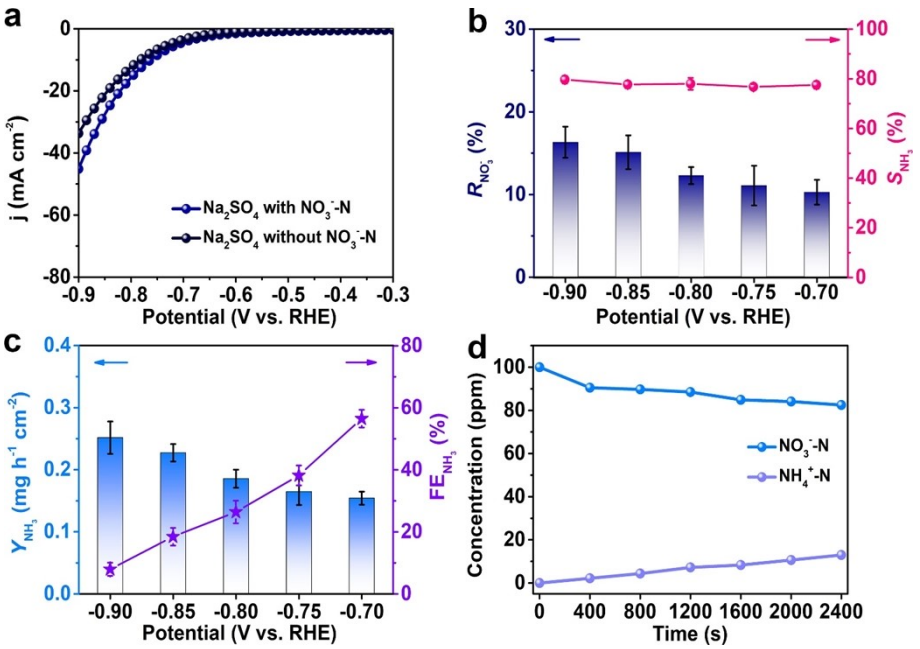

Fig. S19. (a) LSV curves of CoO_x in 0.5 M Na_2SO_4 with and without 100 ppm NO_3^--N. (b) $R_{NO_3^-}$ and S_{NH_3} of CoO_x at different potentials. (c) Y_{NH_3} and FE_{NH_3} of CoO_x at different potentials. (d) Time-dependent concentration change of NO_3^--N and NH_4^+-N over CoO_x at −0.90 V.

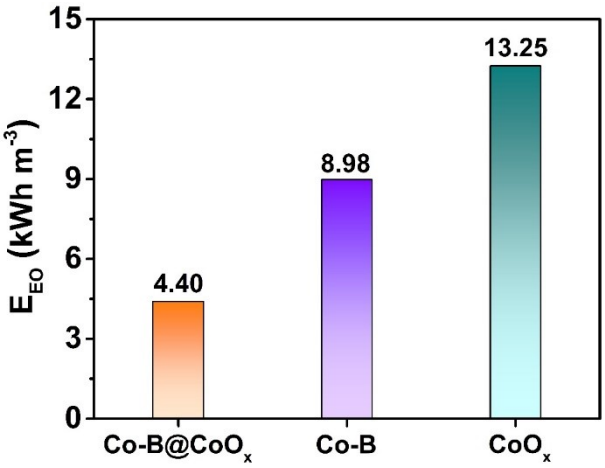

Fig. S20. Comparison of E_{EO} over Co-B@CoO_x, Co-B, and CoO_x at −0.75 V.

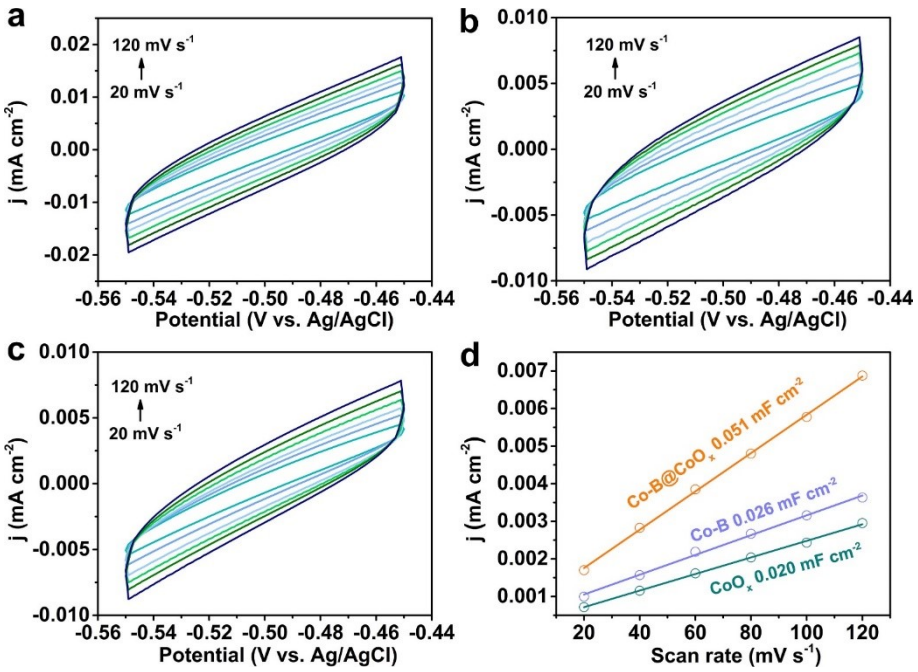

Fig. S21. CV curves of (a) Co-B@CoO_x, (b) Co-B, and (c) CoO_x with scan rates from 20 to 120 mV s^{-1}. (d) Linear fittings of capacitive current densities against the scan rates for Co-B@CoO_x, Co-B, and CoO_x.

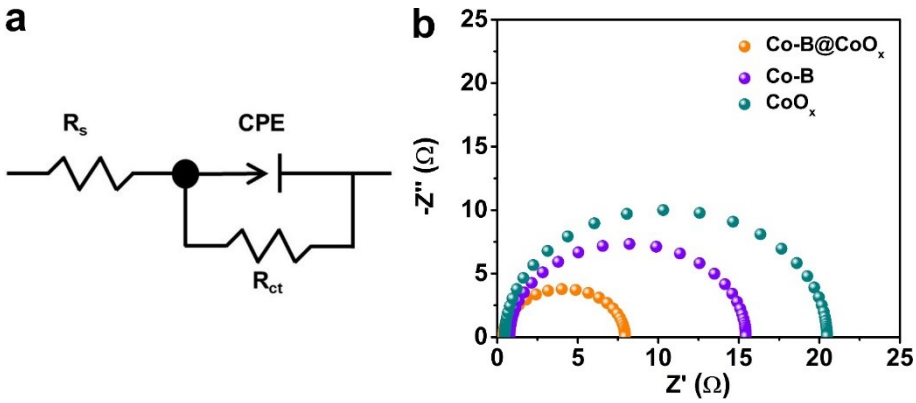

Fig. S22. (a) Equivalent circuit diagram. (b) Nyquist plots of Co-B@CoO_x, Co-B, and CoO_x.

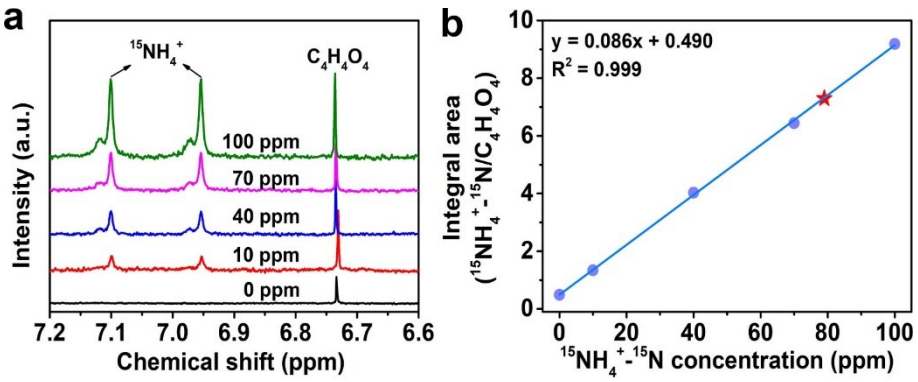

Fig. S23. (a) ^{1}H NMR spectra of standard $^{15}NH_4^+$ solutions with different concentrations. (b) Calibration curve used for the determination of $^{15}NH_4^+$-^{15}N concentration.

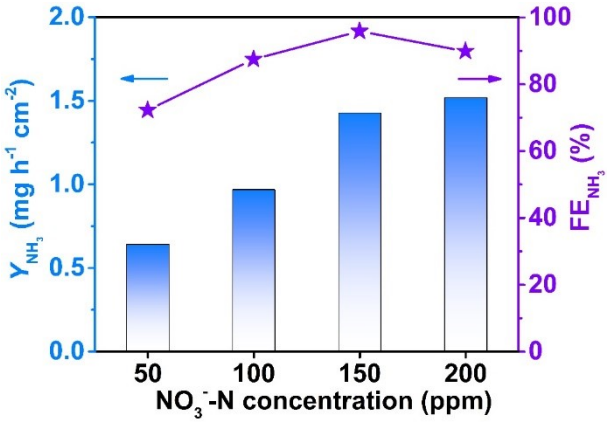

Fig. S24. $^{Y_{NH_3}}$ and $^{FE_{NH_3}}$ over Co-B@CoO_x in 0.5 M Na_2SO_4 with different NO_3^--N concentrations at −0.75 V.

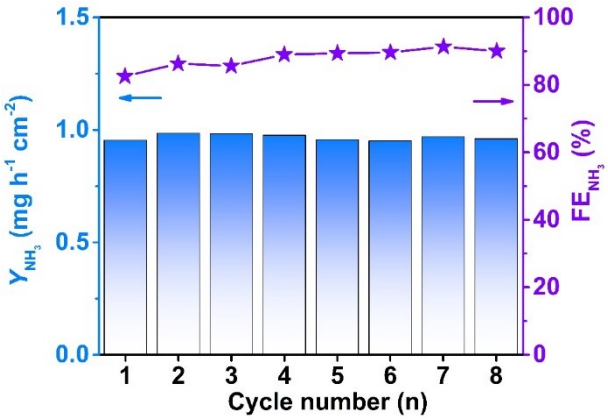

Fig. S25. $^{Y_{NH_3}}$ and $^{FE_{NH_3}}$ over Co-B@CoO_x in consecutive recycling test at −0.75 V.

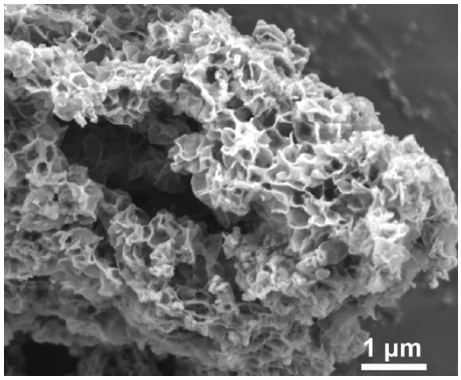

Fig. S26. SEM image of Co-B@CoO_x after long-term electrolysis.

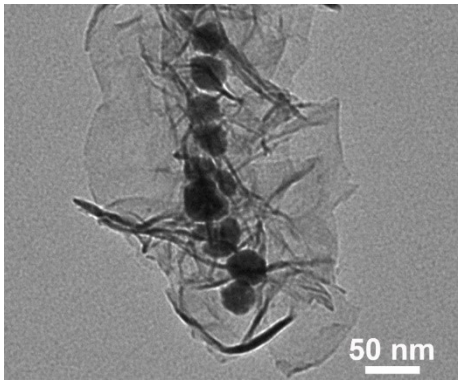

Fig. S27. TEM image of Co-B@CoO_x after long-term electrolysis.

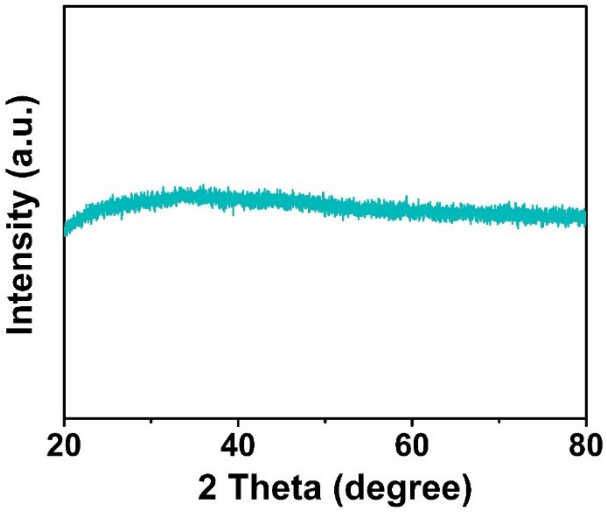

Fig. S28. XRD pattern of Co-B@CoO_x after long-term electrolysis.

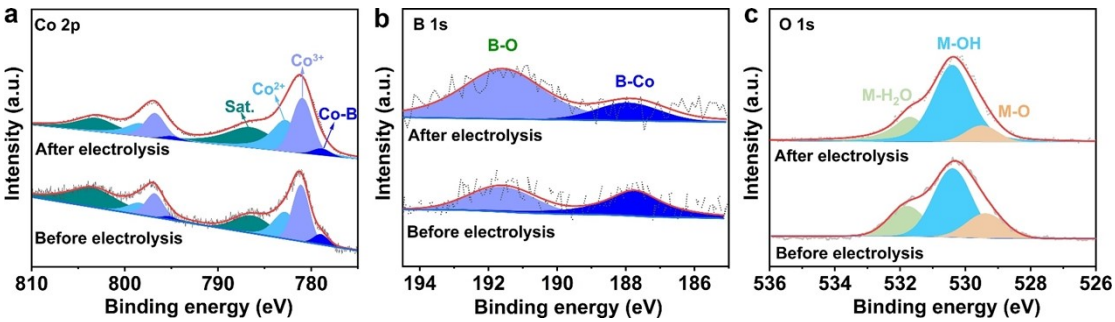

Fig. S29. (a) Co 2p, (b) B 1s, and (c) O 1s XPS spectra of Co-B@CoO_x before and after long-term electrolysis.

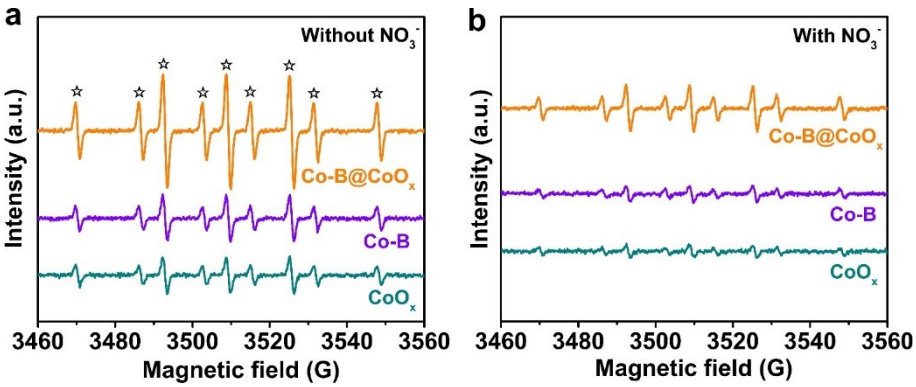

Fig. S30. ESR spectra of the electrolytes obtained after 3 min's electrolysis at −0.75 V by Co-B@CoO_x, Co-B, and CoO_x in 0.5 M Na_2SO_4 electrolyte (a) without and (b) with 100 ppm NO_3^--N.

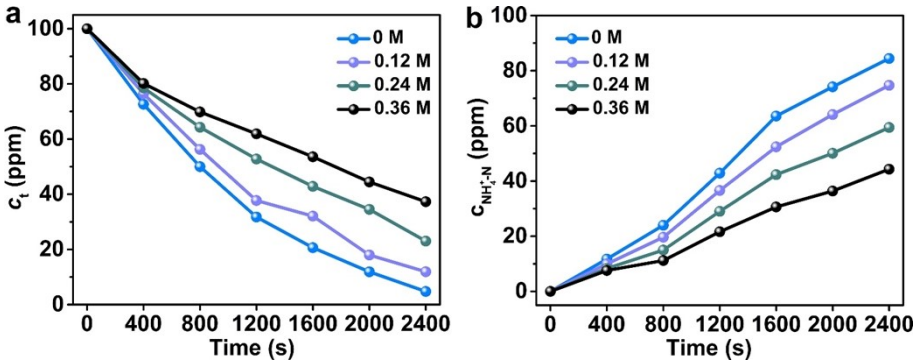

Fig. S31. Concentration changes of (a) NO_3^--N and (b) NH_4^+-N versus electrolysis time on Co-B@CoO_x with different concentrations of TBA at −0.90 V.

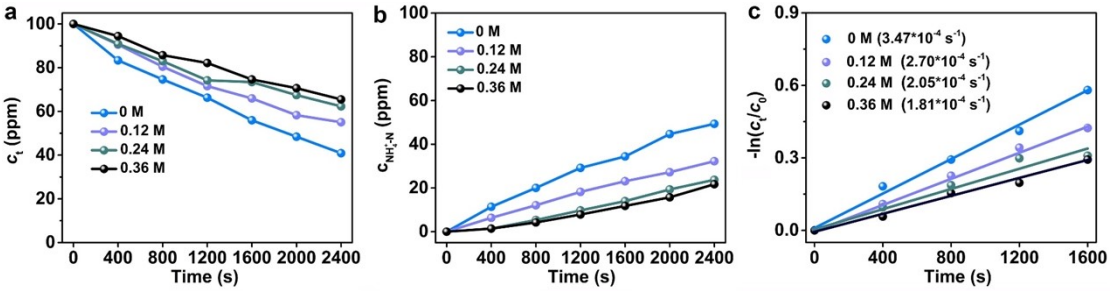

Fig. S32. Concentration changes of (a) NO_3^--N and (b) NH_4^+-N versus electrolysis time on Co-B with different concentrations of TBA at −0.90 V. (c) Linearized pseudo first-order kinetic profiles of Co-B with different concentrations of TBA.

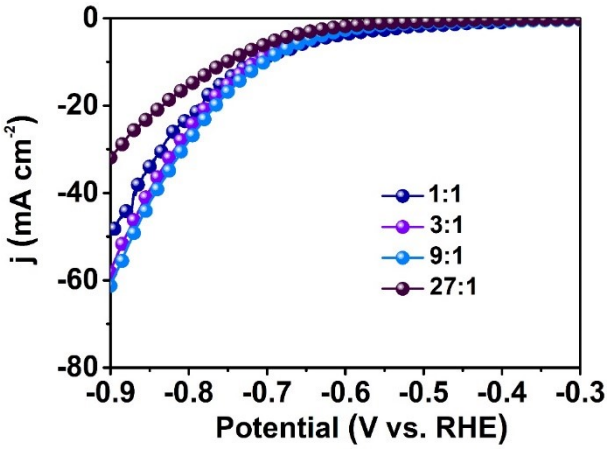

Fig. S33. LSV curves of physical mixtures of Co-B and CoO_x with different weight ratios ($m_{Co\text{-}B}/m_{CoOx}$) in 0.5 M Na_2SO_4 containing 100 ppm NO_3^--N.

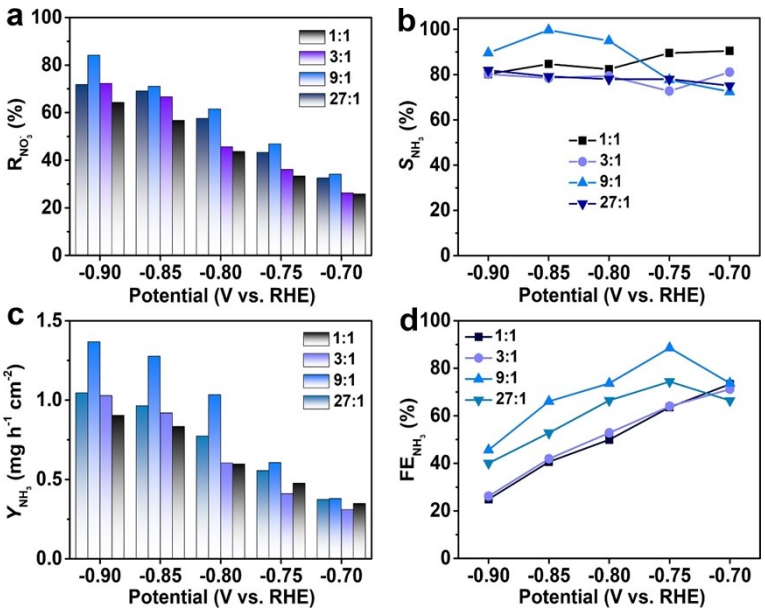

Fig. S34. (a) $R_{NO_3^-}$, (b) S_{NH_3}, (c) Y_{NH_3}, and (d) FE_{NH_3} of physical mixtures of Co-B and CoO_x with different weight ratios ($m_{Co\text{-}B}/m_{CoOx}$) at different potentials.

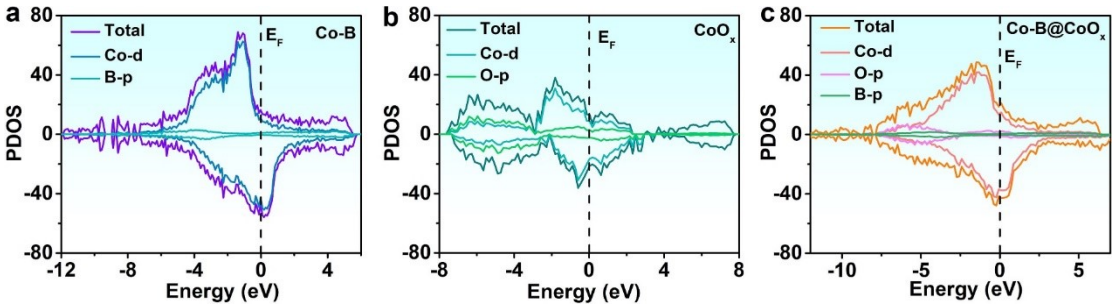

Fig. S35. PDOS profiles for (a) Co-B, (b) CoO_x, and (c) Co-B@CoO_x.

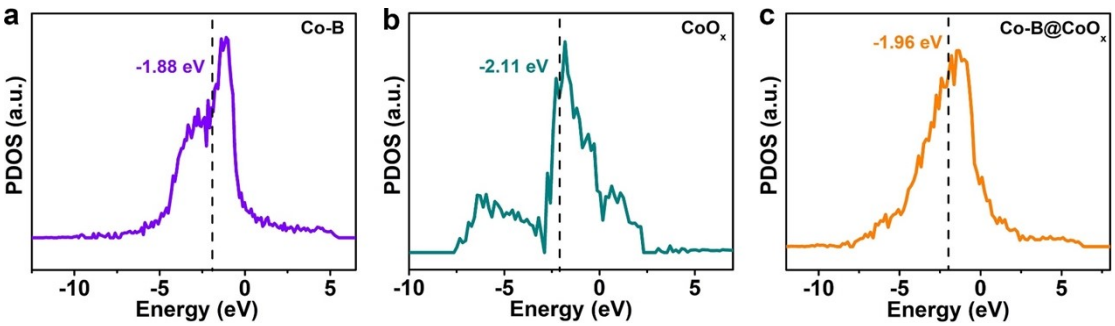

Fig. S36. PDOS profiles of Co-d band for (a) Co-B, (b) CoO_x, and (c) Co-B@CoO_x.

The vertical dashed lines indicate the position of the d-band center.

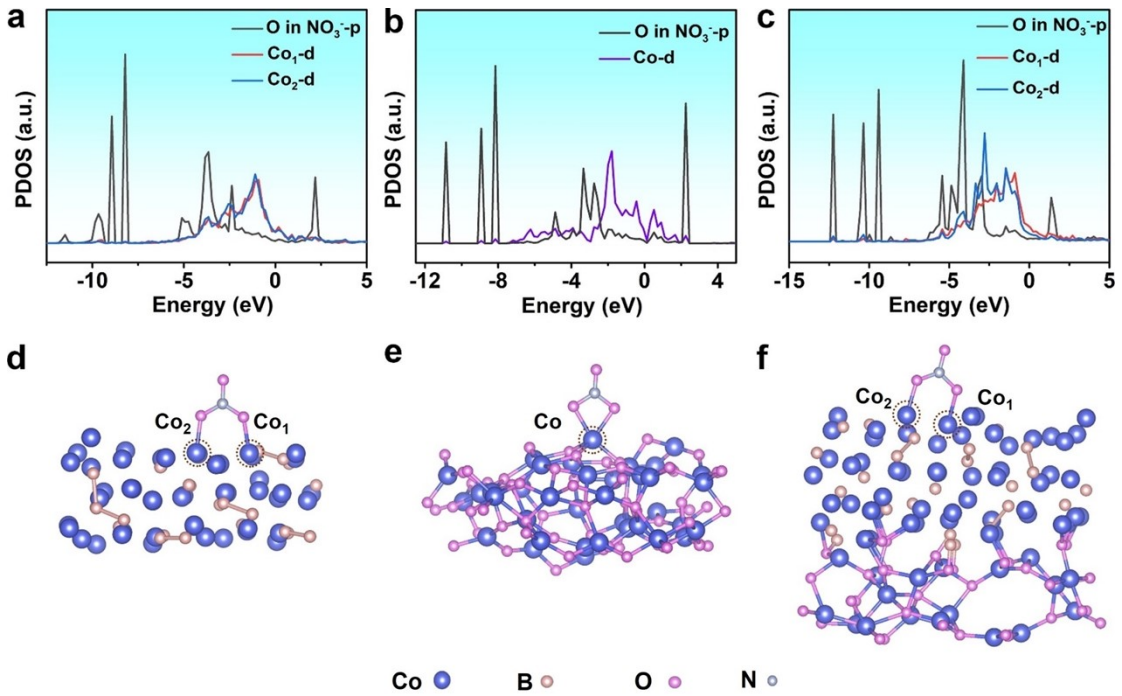

Fig. S37. PDOS profiles of O p and Co d orbitals for NO_3^- adsorption on (a) Co-B, (b) CoO_x, and (c) Co-B@CoO_x. Structure models depicting the adsorption of NO_3* on (d) Co-B, (e) CoO_x, and (f) Co-B@CoO_x.

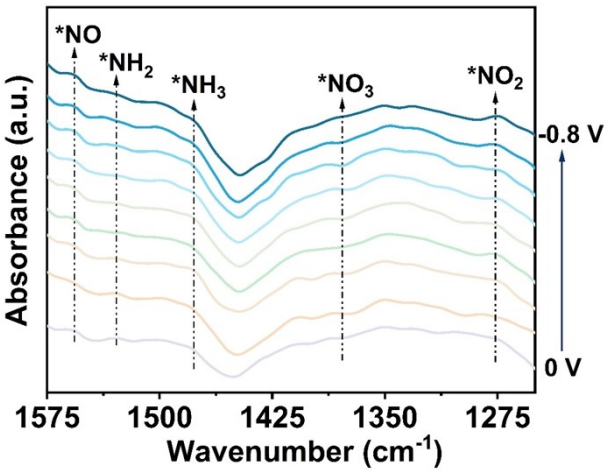

Fig. S38. The *in-situ* ATR-SEIRAS spectra of Co-B@CoO_x.

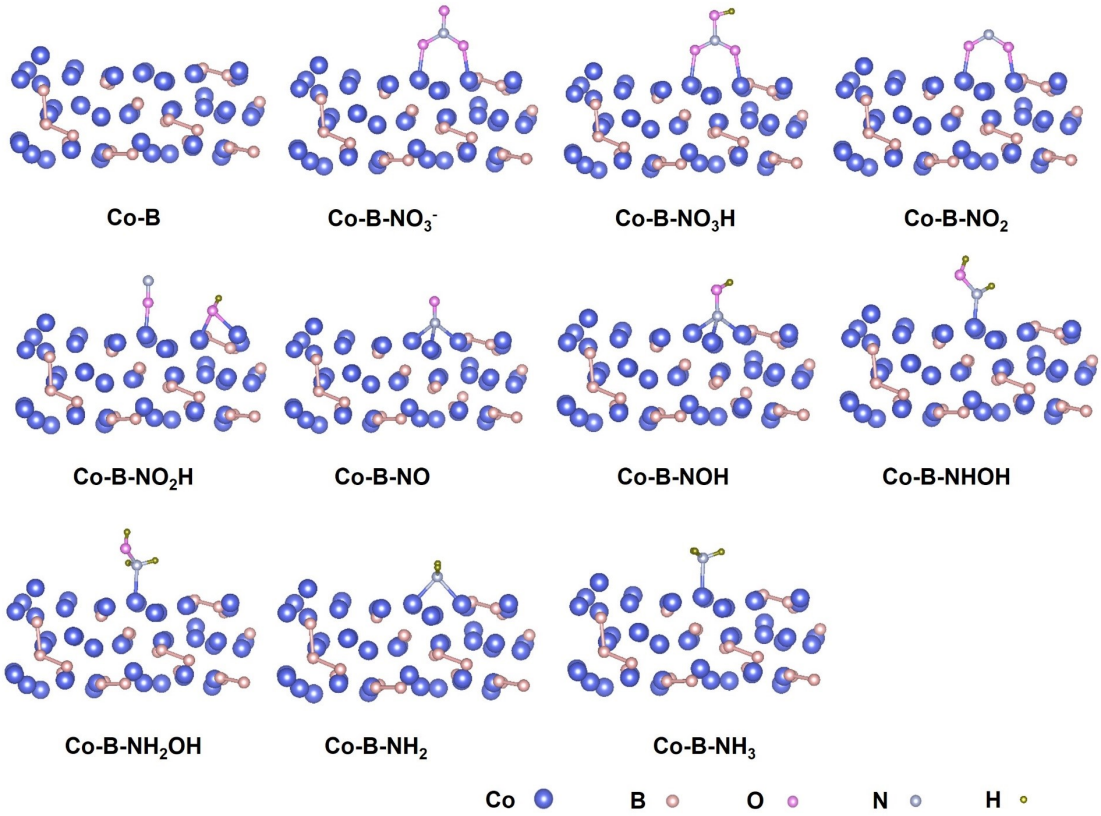

Fig. S39. Optimized structure models of NO_3RR intermediates adsorbed on Co-B.

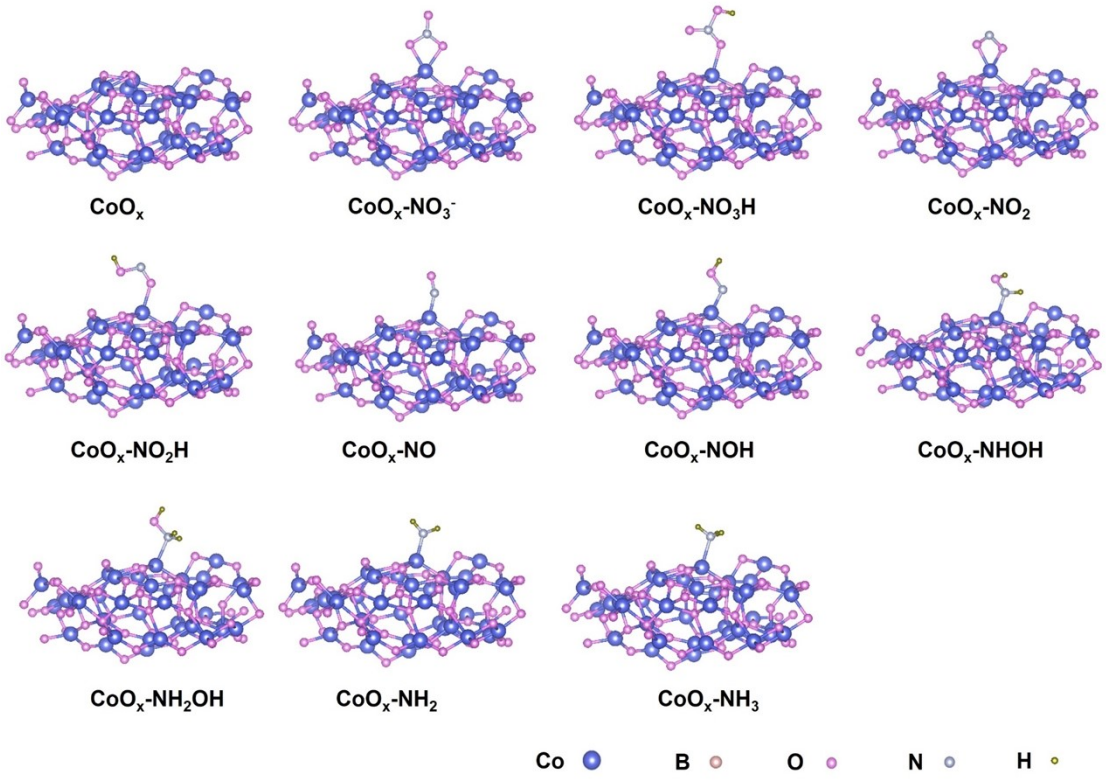

Fig. S40. Optimized structure models of NO_3RR intermediates adsorbed on CoO_x.

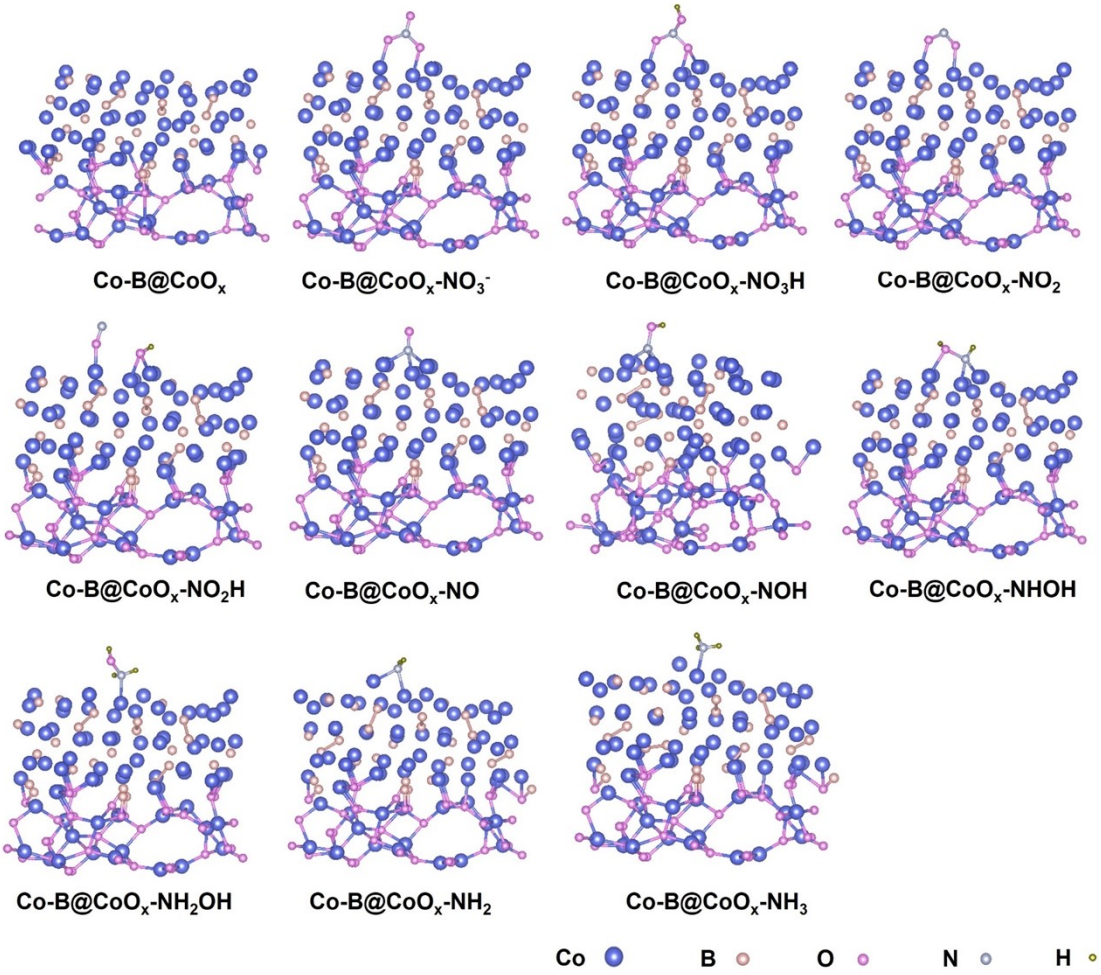

Fig. S41. Optimized structure models of NO_3RR intermediates adsorbed on Co-B@CoO_x.

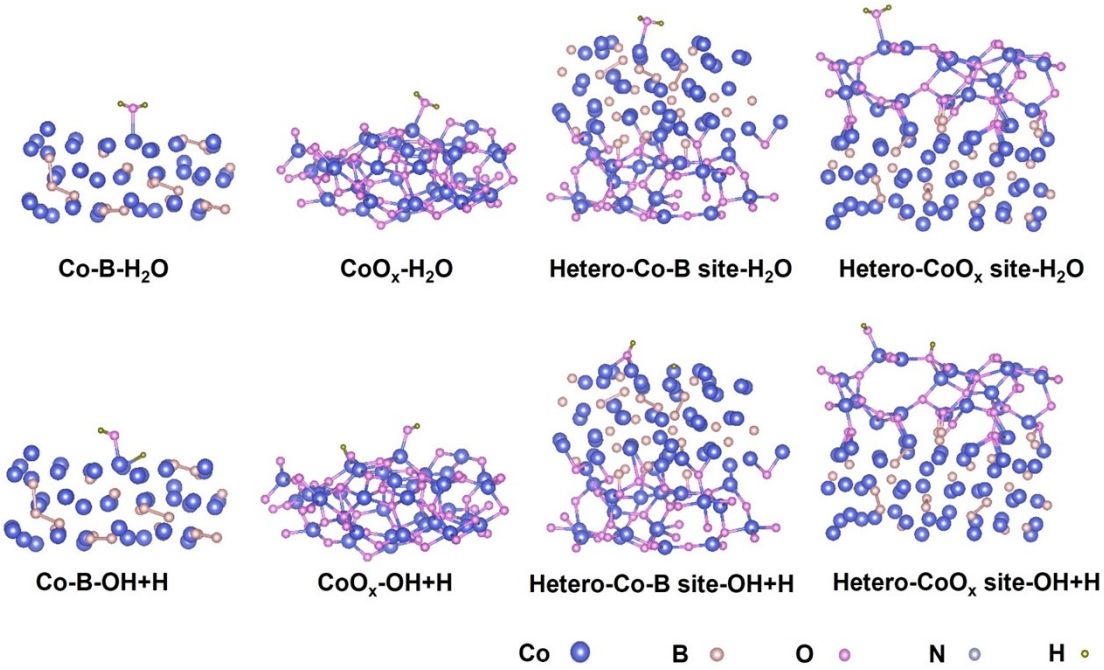

Fig. S42. Optimized structure models of adsorbed H_2O, OH+H on Co-B, CoO_x, hetero-Co-B site and hetero-CoO_x site of Co-B@CoO_x.

Supplementary Tables

Samples	Shell	CN	R(Å)	σ^2(Å^2)	ΔE_0	R factor
Co-B@CoO_x	Co-O	1.9±0.2	1.91±0.01	0.0031	6.1±1.3	0.0017
	Co-B	1.4±0.3	2.10±0.04	0.0023		
	Co-Co (Co-B)	4.4±0.3	2.54±0.01	0.0170		
	Co-Co (CoO_x)	2.2±0.2	2.82±0.01	0.0066		
Co-B	Co-B	4.9±0.3	2.11±0.01	0.0081	6.7±1.7	0.0020
	Co-Co	5.7±0.3	2.50±0.01	0.0164		
CoO_x	Co-O	4.1±0.1	1.92±0.01	0.0034	2.4±0.4	0.0022
	Co-Co	2.8±0.1	2.86±0.01	0.0034		
Co foil	Co-Co	12*	2.49±0.01	0.0064	7.5±0.3	0.0016
CoO	Co-O	5.9±0.6	2.10±0.01	0.0094	2.5±0.9	0.0087
	Co-Co	12.5±0.6	3.01±0.01	0.0087		
Co_2O_3	Co-O	4.7±0.2	1.91±0.01	0.0025	7.4±0.6	0.0033
	Co-Co	5.3±0.2	2.86±0.01	0.0054		

Table S1. EXAFS fitting parameters at Co K-edge for various samples (S_0^2 = 0.82).

CN: coordination numbers. R(Å): bond distance. σ^2(Å^2): Debye-Waller factors. ΔE_0: the inner potential correction. R factor: goodness of fit. S_0^2 was set to 0.82 according to the experimental EXAFS fit of Co foil reference by fixing CN as the known crystallographic value. δ: percentage. *This value was fixed during EXAFS fitting, based on the known structure of Co.

Table S2. Comparison of electrocatalytic NO_3RR performance for Co-B@CoO_x at −0.75 V and other metal-based electrocatalysts under ambient conditions.

Catalyst	Electrolyte	Performance	Ref.
Co-B@CoO_x	**0.5 M Na_2SO_4 +100 ppm NO_3^--N (pH=3)**	**Y_{NH_3}: 0.96 mg h^{-1} cm^{-2} FE_{NH_3}: 86.82%**	**This work**
CuCl-BEF	0.5 M Na_2SO_4 +22.58 ppm NO_3^--N	Y_{NH_3}: 1.82 mg h^{-1} cm^{-2} FE_{NH_3}: 44.7%	10
Co_3O_4@NiO HNTs	0.5 M Na_2SO_4 +200 ppm NO_3^--N	Y_{NH_3}: 0.08 mg h^{-1} cm^{-2} FE_{NH_3}: 54.97%	11
Cu@$Cu_{2+1}O$	0.5 M K_2SO_4 +50 ppm NO_3^--N	Y_{NH_3}:0.57 mg h^{-1} cm^{-2} FE_{NH_3}: 87.07%	12
PdCoO/NF	0.5 M K_2SO_4 +200 ppm NO_3^--N	Y_{NH_3}: 3.47 mg h^{-1} cm^{-2} FE_{NH_3}: 88.6%	13
Cu-PTCDA	0.1 M PBS +112.90 ppm NO_3^--N	Y_{NH_3}: 0.44 mg h^{-1} cm^{-2} FE_{NH_3}: 85.9%	14
$BimNTf_2$-Co_3O_{4-x}	0.1 M Na_2SO_4 +112.90 ppm NO_3^--N	Y_{NH_3}: 9.07 mg h^{-1} cm^{-2} FE_{NH_3}: 84.74%	15
Ni-NSA-V_{Ni}	0.2 M Na_2SO_4 +45.16 ppm NO_3^--N	Y_{NH_3}: 4.01 mg h^{-1} cm^{-2} FE_{NH_3}: 88.9%	16
TiO_{2-x}	0.5 M Na_2SO_4 +50 ppm NO_3^--N	Y_{NH_3}: 0.77 mg h^{-1} cm^{-2} FE_{NH_3}: 85.0%	17
Cu@C	1 M KOH +14 ppm NO_3^--N	Y_{NH_3}: 0.47 mg h^{-1} cm^{-2} FE_{NH_3}: 72.0%	18
a-RuO_2	0.5 M Na_2SO_4 +200 ppm NO_3^--N	Y_{NH_3}: 1.97 mg h^{-1} cm^{-2} FE_{NH_3}: 97.46%	19
Ru-$Co(OH)_2$	1 M KOH +200 ppm NO_3^--N	Y_{NH_3}: 4.15 mg h^{-1} cm^{-2} FE_{NH_3}: 94.3%	20
$Cu_{1.5}$/NTC/(CuN_4&Cu_4)	0.5 M Na_2SO_4 +11.29 ppm NO_3^--N	Y_{NH_3}: 0.75 mg h^{-1} cm^{-2} FE_{NH_3}: 94.3%	21
Ru@C_3N_4/Cu	0.5 M Na_2SO_4 +45.16 ppm NO_3^--N	Y_{NH_3}: 1.05 mg h^{-1} cm^{-2} FE_{NH_3}: 91.3%	22

Catalyst	NO_3^--N concentration (ppm)	EC (kWh $mol_{NO_3}^{-1}$)	E_{EO} (kWh m^{-3})	Ref.
Co-B@CoO_x	**100**	**0.39**	**4.40**	**This work**
Fe_{SAs}	50	0.34	1.89	1
Cu/Fe-TiO_2	11.29	0.54	0.73	23
SCF	100	0.66	3.78	24
Cu_2O/Cu	30	1.29	-	25
FeNi	50	1.60	5.7	26
Ni-Fe^0/Fe_3O_4	50	4.42	-	27
Cu/GO/Ti	50	7.99	-	28

Table S3. Comparison of energy consumption for NO_3^- removal for Co-B@CoO_x with other electrocatalysts under ambient conditions.

Table S4. Comparison of Zn-NO_3^- battery performance based on Co-B@CoO_x and other electrocatalysts under ambient conditions.

Catalyst	NO_3^--N concentration (ppm)	Power density (mW cm^{-2})	Performance	Ref.
Co-B@CoO_x	**100**	**4.78**	**Y_{NH_3}: 0.89 mg h^{-1} cm^{-2} FE_{NH_3}: 85.4%**	**This work**
Pd/TiO_2	3500	0.87	Y_{NH_3}: 0.54 mg h^{-1} cm^{-2} FE_{NH_3}: 81.3%	29
CoP-Ni_2P	50	1.05	Y_{NH_3}: 0.21 mg h^{-1} cm^{-2} FE_{NH_3}: 76.23%	30
Pd/CoP	50	1.55	Y_{NH_3}: 0.27 mg h^{-1} cm^{-2} FE_{NH_3}: 86.76%	31
RuFe NFs	1400	1.9	/	32
Cu-LC-10	1016	3.1	/	33
$Co_2B@Co_3O_4$ /TM	1400	3.21	Y_{NH_3}: 0.74 mg h^{-1} cm^{-2} FE_{NH_3}: 97.2%	34
Fe/Ni_2P	700	3.25	Y_{NH_3}: 0.38 mg h^{-1} cm^{-2} FE_{NH_3}: 85.0%	35
Ni/Co-MOFs	1400	3.66	Y_{NH_3}: 1.12 mg h^{-1} cm^{-2} FE_{NH_3}: 99.4%	36
$NiCo_2O_4$/CC	1400	3.94	Y_{NH_3}: 0.85 mg h^{-1} cm^{-2} FE_{NH_3}: 96.1%	37
GB Ni NPs	14000	4.2	/	38
PdCuAg MTs	140	4.8	Y_{NH_3}: 0.44 mg h^{-1} cm^{-2} FE_{NH_3}: 92.4%	39
Fe_2TiO_5	1400	5.6	Y_{NH_3}: 0.78 mg h^{-1} cm^{-2} FE_{NH_3}:70.15%	40

References

1 Q. Song, M. Li, X. Hou, J. Li, Z. Dong, S. Zhang, L. Yang and X. Liu, *Appl. Catal.*, *B*, 2022, **317**, 121721.

2 S. Han, H. Li, T. Li, F. Chen, R. Yang, Y. Yu and B. Zhang, *Nat. Catal.*, 2023, **6**, 402–414.

3 G. Kresse and J. Furthmüller, *Phys. Rev. B*, 1996, **54**, 11169–11186.

4 G. Kresse and J. Hafner, *Phys. Rev. B*, 1993, **47**, 558–561.

5 B. Hammer, L. B. Hansen and J. K. Nørskov, *Phys. Rev. B*, 1999, **59**, 7413–7421.

6 J. P. Perdew, K. Burke and M. Ernzerhof, *Phys. Rev. Lett.*, 1996, **77**, 3865–3868.

7 P. E. Blöchl, *Phys. Rev. B*, 1994, **50**, 17953–17979.

8 J. Klimeš, D. R. Bowler and A. Michaelides, *Phys. Rev. B*, 2011, **83**, 195131.

9 S. Grimme, J. Antony, S. Ehrlich and H. A. Krieg, *J. Chem. Phys.*, 2010, **132**, 154104.

10 W.-J. Sun, H.-Q. Ji, L.-X. Li, H.-Y. Zhang, Z.-K. Wang, J.-H. He and J.-M. Lu, *Angew. Chem.*, *Int. Ed.*, 2021, **60**, 22933–22939.

11 Y. Wang, C. Liu, B. Zhang and Y. Yu, *Sci. China Mater.*, 2020, **63**, 2530–2538.

12 T. Ren, K. Ren, M. Wang, M. Liu, Z. Wang, H. Wang, X. Li, L. Wang and Y. Xu, *Chem. Eng. J.*, 2021, **426**, 130759.

13 M. Liu, Q. Mao, K. Shi, Z. Wang, Y. Xu, X. Li, L. Wang and H. Wang, *ACS Appl. Mater. Interfaces*, 2022, **14**, 13169−13176.

14 G.-F. Chen, Y. Yuan, H. Jiang, S.-Y Ren, L.-X. Ding, L. Ma, T. Wu, J. Lu and H. Wang, *Nat. Energy*, 2020, **5**, 605–613.

15 D. Qin, S. Song, Y. Liu, K. Wang, B. Yang and S. Zhang, *Angew. Chem.*, *Int. Ed.*, 2023, **62**, e202304935.

16 C. Wang, W. Zhou, Z. Sun, Y. Wang, B. Zhang and Y. Yu, *J. Mater. Chem. A*, 2021, **9**, 239–243.

17 R. Jia, Y. Wang, C. Wang, Y. Ling, Y. Yu and B. Zhang, *ACS Catal.*, 2020, **10**, 3533–3540.

18 Z. Song, Y. Liu, Y. Zhong, Q. Guo, J. Zeng and Z. Geng, *Adv. Mater.*, 2022, **34**, 2204306.

19 Y. Wang, H. Li, W. Zhou, X. Zhang, B. Zhang and Y. Yu, *Angew. Chem.*, *Int. Ed.*, 2022, **134**, e202202604.

20 T. Ren, Z. Yu, H. Yu, K. Deng, Z. Wang, X. Li, H. Wang, L. Wang and Y. Xu, *ACS Nano*, 2023, **17**, 12422–12432.

21 X.-Y. Ji, K. Sun, Z.-K. Liu, X. Liu, W. Dong, X. Zuo, R. Shao and J. Tao, *Nano-Micro Lett.*, 2023, **15**, 110.

22 Y. Zheng, M. X. Qin, X. Yu, H. Yao, W. Zhang, G. Xie and X. Guo, *Small*, 2023, **19**, 2302266.

23 X. Yang, R. Wang, S. Wang, C. Song, S. Lu, L. Fang, F. Yin and H. Liu, *Appl. Catal.*, *B*, 2023, **325**, 122360.

24 L. Fang, S. Wang, C. Song, S. Lu, X. Yang, X. Qi and H. Liu, *Chem. Eng. J.*, 2022, **446**, 137341.

25 J. Zhou, F. Pan, Q. Yao, Y. Zhu, H. Ma, J. Niu and J. Xie, *Appl. Catal.*, *B*, 2022, **317**, 121811.

26 X. Chen, T. Zhang, M. Kan, D. Song, J. Jia, Y. Zhao and X. Qian, *Environ. Sci. Technol.*, 2020, **54**, 13344–13353.

27 Z. A. Jonoush, A. Rezaee and A. Ghaffarinejad, *J. Clean. Prod.*, 2020, **242**, 118569.

28 J. Wang, S. Wang, Z. Zhang and C. Wang, *J. Environ. Manage.*, 2020, **276**, 111357.

29 Y. Guo, R. Zhang, S. Zhang, Y. Zhao, Q. Yang, Z. Huang, B. Dong and C, Zhi, *Energy Environ. Sci.*, 2021, **14**, 3938–3944.

30 Y. Gao, K. Wang, C. Xu, H. Fang, H. Yu, H. Zhang, S. Li, C. Li and F. Huang, *Appl. Catal.*, *B*, 2023, **330**, 122627.

31 Y. Gao, K. Wang, S. Li, H. Zhang and F. Huang, *J. Mater. Chem. A*, 2023, **11**, 21161–21169.

32 Y. Wang, M. Sun, J. Zhou, Y. Xiong, Q. Zhang, C. Ye, X. Wang, P. Lu, T. Feng, F. Hao, F. Liu, J. Wang, Y. Ma, J. Yin, S. Chu, L. Gu, B. Huang and Z. Fan, *Proc. Natl. Acad. Sci. U. S. A.*, 2023, **120**, e2306461120.

33 K. Huang, K. Tang, M. Wang, Y. Wang, T. Jiang and M. Wu, *Adv. Funct. Mater.*, 2024, **14**, 2315324.

34 L. Xie, S. Sun, L. Hu, J. Chen, J. Li, L. Ouyang, Y. Luo, A. A. Alshehri, Q. Kong, Q. Liu and X. Sun, *ACS Appl. Mater. Interfaces*, 2022, **14**, 49650−49657.

35 R. Zhang, Y. Guo, S. Zhang, D. Chen, Y. Zhao, Z. Huang, L. Ma, P. Li, Q. Yang, G. Liang and C. Zhi, *Adv. Energy Mater.*, 2022, **12**, 2103872.

36 J. Ma, Y. Zhang, B. Wang, Z. Jiang, Q. Zhang and S. Zhuo, *ACS Nano*, 2023, **17**, 6687–6697.

37 Q. Liu, L. Xie, J. Liang, Y. Ren, Y. Wang, L. Zhang, L. Yue, T. Li, Y. Luo, N. Li, B. Tang, Y. Liu, S. Gao, A. A. Alshehri, I. Shakir, P. O. Agboola, Q. Kong, Q. Wang, D. Ma and X. Sun, *Small*, 2022, **18**, 2106961.

38 J. Zhou, M. Wen, R. Huang, Q. Wu, Y. Luo, Y. Tian, G. Wei and Y. Fu, *Energy Environ. Sci.*, 2023, **16**, 2611–2620.

39 L. Sun, H. Yao, Y. Wang, C. Zheng and B. Liu, *Adv. Energy Mater.*, 2023, **13**, 2303054.

40 H. Du, H. Guo, K. Wang, X. Du, B. A. Beshiwork, S. Sun, Y. Luo, Q. Liu, T. Li and X. Sun, *Angew. Chem.*, *Int. Ed.*, 2023, **135**, e202215782.